Nanoscale

PAPER

View Article Online
View Journal | View Issue

Open Access Article. Published on 29 June 2015. Downloaded on 12/4/2025 5:40:46 PM.
This article is licensed under a Creative Commons Attribution-NonCommercial 3.0 Unported Licence.

Cite this: *Nanoscale*, 2015, **7**, 12906

Enhancing the performance of catalytic AuPt nanoparticles in nonaqueous lithium–oxygen batteries†

Meihua Lu,[a] Dongyun Chen,[b] Chaohe Xu,[a] Yi Zhan[a] and Jim Yang Lee*[a]

Received 10th May 2015,
Accepted 25th June 2015

DOI: 10.1039/c5nr03061g

www.rsc.org/nanoscale

The deposition of catalytic AuPt (1 : 1) nanoparticles (NPs) into hollow mesoporous nitrogen-doped carbon microspheres (HMCMS) was found to significantly improve the effectiveness of the catalysis of oxygen reactions in nonaqueous lithium–oxygen batteries (LOBs); surpassing the performance of unsupported AuPt NPs or HMCMS in discharge and charge overpotentials (lower), specific capacity and rate performance (higher), and cycle life (longer). Specifically at a typical current density of 100 mA g^{-1}, a LOB with the AuPt/HMCMS cathode catalyst could provide discharge and charge capacities of 6028 and 6000 mA h g^{-1} respectively and a charge–discharge voltage gap of only 1.27 V. The discharge capacity decreased by 5% when the current density was doubled, and by 23% when the current density was quintupled. The AuPt/HMCMS LOB could be cycled 75 times for a depth of discharge (DOD) of 1000 mA h g^{-1} without exceeding the charge cut-off voltage of 4.4 V. These measurements indicate that the HMCMS is an outstanding catalyst support to use for increasing the effectiveness of oxygen electrocatalysts in the LOBs.

Introduction

The extraordinarily high theoretical energy density of nonaqueous lithium–oxygen batteries (LOBs) (~5200 Wh kg^{-1} including the mass of oxygen is about 20 fold the energy density of current Li-ion batteries) is a lure for the large scale storage of electrical energy.[1–3] In a typical nonaqueous LOB, Li^+ reacts with oxygen to form insoluble Li_2O_2 (reversible to charging) or Li_2O (irreversible to charging) during discharge, which is deposited and accumulated in the cathode. Since these lithium oxides are insulators, they can impede the discharge process by reducing the conductivity and the free volume of the cathode. During charging, the Li_2O_2 in the cathode decomposes to oxygen, and Li^+ is released and returned to the Li anode. The oxygen cathode should therefore not only be catalytic for the oxygen reduction reaction (ORR) during discharge and the oxygen evolution reaction (OER) during charge, but also contain adequate porosity and electrical conductivity to sustain oxygen diffusion, electrolyte permeation, electron transport and the accumulation of lithium oxides. Research over the years has shown that catalysts with a balanced mixture of mesopores and macropores are conducive for high specific capacity.[4] Such a hierarchical pore structure is most easily fabricated from carbon materials which, in addition to their low cost, are also notably electrically conductive with some ORR activity in non-aqueous solution. Increasing interest in using mesoporous carbon for the LOB cathode can be demonstrated by a quick sampling of the recent literature.[5–12] In most cases, the authors attributed the good performance to a dual pore architecture where the mesopores promote Li^+ and oxygen diffusion and electrolyte permeation, and the macropores provide the free volume to store the discharge product (solid Li_2O_2). The mesoporous/macroporous dual pore carbon catalysts are not perfect: the cell capacity is significantly lower than the theoretical capacity of LOBs, and there are large discharge and charge overpotentials resulting in an unsatisfactory cycle life. These deficiencies can be attributed to the inadequate catalytic OER activity of carbon and the low electrical conductivity of carbon in these constructions.

The electrical and electrochemical properties of carbon can be improved by nitrogen-doping of carbon and/or incorporating a more OER-active or a bifunctional (*i.e.* active for both ORR and OER) catalyst into carbon. Nitrogen-doped carbons have shown higher electrical conductivity and ORR activity, and greater stability to cycling than un-doped carbon.[13–15] For example the specific capacity of carbon nanotubes for LOBs could be increased by 50% through nitrogen doping.[16] Smaller discharge overpotential and higher capacity were also reported

[a]*Department of Chemical and Biomolecular Engineering, National University of Singapore, 10 Kent Ridge Crescent, Singapore 119260, Singapore.*
E-mail: cheleejy@nus.edu.sg; Fax: +65-67791936; Tel: +65-65162899
[b]*College of Chemistry, Chemical Engineering and Materials Science, Soochow University, Suzhou, 215123, China*

† Electronic supplementary information (ESI) available: TEM, BET, XRD and XPS of the AuPt/HMCMS composite. See DOI: 10.1039/c5nr03061g

This journal is © The Royal Society of Chemistry 2015

Open Access Article. Published on 29 June 2015. Downloaded on 12/4/2025 5:40:46 PM.
This article is licensed under a Creative Commons Attribution-NonCommercial 3.0 Unported Licence.

for LOBs using a nitrogen-doped mesoporous carbon cathode ("Black Pearl 2000").

There are more effective ORR and OER catalysts than carbon. Noble metals and their alloys or oxides such as Pd,[17,18] Pt,[19] Ru,[20,21] AuPt,[22] Pt_xCo_y [23] and RuO_2 [24,25] are all more ORR and OER active than carbon in nonaqueous LOBs. The AuPt NPs in particular have shown very impressive bifunctional properties in nonaqueous oxygen electrocatalysis. The noble metal NPs are normally administered as a supported catalyst system on a conducting substrate. Carbon black and carbon nanotubes (but not hierarchically structured porous carbon) were used in the above mentioned studies but the rate performance of the resulting LOBs is still an area for improvement.

We posit that a combination of AuPt NPs and nitrogen-doped carbon with a dual pore architecture may provide the best synergy of functions. The mesoporous/macroporous carbon implemented in this study was in the form of hollow mesoporous nitrogen-doped carbon microspheres (HMCMS) which are very different from the common sheet-like mesoporous carbons in the literature. The latter are more predisposed to aggregation during electrode fabrication and discharge and charge processes, leading to a gradual loss of the pore volume. A mesoporous carbon with an overall spherical geometry would reduce such propensity. The efficient transport of electrons, electrolytes, and oxygen during discharge enabled Li_2O_2 to be deposited as a thin and uniform film on the conducting surface of HMCMS. OER was made easier with the film-like Li_2O_2 in close contact with the conducting surface due to the lowering of the overall charge transfer resistance. In addition the HMCMS also served as a supplemental ORR catalyst in nonaqueous oxygen electrocatalysis. As a result, LOBs with the AuPt/HMCMS composite catalyst cathode delivered very satisfying performance in terms of capacity (higher), discharge and charge polarizations (smaller) and cycle life (longer). The composite catalyst easily surpassed the performance of HMCMS and unsupported AuPt NP catalysts, and their capacity and rate performance are also improvements over AuPt NPs supported on Vulcan XC-72 carbon.[22]

Experimental section

Chemicals

Hydrogen tetrachloroaurate trihydrate ($HAuCl_4{\cdot}3H_2O$), chloroplatinic acid hexahydrate ($H_2PtCl_6{\cdot}6H_2O$, ≥37.50% Pt basis), and sodium borohydride (98%) from Alfa Aesar; hydrogen fluoride (48%), ammonia solution (32 wt%) and acetonitrile (HPLC grade) from Merck; tetraethyl orthosilicate (TEOS, >99%), trimethoxy(octadecyl)silane (C_{18}TMOS, 90%), dopamine hydrochloride, tris(hydroxymethyl)aminomethane (THAM, 99.8%), tetraethylene glycol dimethyl ether (TEGDME, ≥99%), polyvinylidene fluoride (PVDF), *N*-methyl-2-pyrrolidone (NMP), lithium trifluoromethanesulfonate ($LiCF_3SO_3$, 99.995% trace metal basis) from Sigma-Aldrich; Ketjen Black (KB, Ketjen Black International, ECP600JD) from MTI were all used as received.

Synthesis of hollow mesoporous nitrogen-doped carbon microspheres (HMCMS)

The synthesis of hollow mesoporous silica microspheres (HMSMS) was based on a previously reported hard templating method.[26] In brief, 58.5 g ethanol and 10 g deionized water (DI water) were mixed in a flask, followed by the addition of 3.10 g aqueous ammonia with stirring. 5.6 mL TEOS was introduced 30 min later under vigorous mixing. The mixture was left to rest for 1 h to form uniform nonporous silica spheres. A mixture of 4.17 g TEOS and 1.87 g C_{18}TMOS was then introduced dropwise under stirring. At the end of addition the mixture was stored at room temperature for 3 h without stirring. The precipitate was centrifuged, vacuum dried at 60 °C, and calcined at 550 °C for 6 h in air. The residual ammonia in the calcined powder was neutralized with 1 M HCl solution and the solid was vacuum dried.

The HMSMS prepared above were then coated with conductive carbon by a dopamine polymerization method. 100 mg HMSMS powder was washed twice with a 50 mmol tri(hydroxymethyl)aminomethane buffer (TRIS buffer, PH = 8.5), and transferred to a flask. 40 mL of 50 mmol TRIS buffer and 80 mg dopamine were added, and the mixture was vigorously stirred for 24 h. The solution turned brown after the formation of polydopamine. The solid product was collected by centrifugation, washed thrice with TRIS buffer, and then vacuum dried at 60 °C overnight. HMCMS were obtained by etching the PDA-coated HMSMS in 10% HF solution for 2 h. The HMCMs were centrifuged and vacuum dried.

Synthesis of the AuPt (1 : 1)/HMCMS composite

10.7 mg HMCMS was mixed with 5 mL of 50 mmol $HAuCl_4$ solution and 5 mL of 50 mmol H_2PtCl_6 solution. The mixture was homogenized for 30 min. An excess of freshly prepared $NaBH_4$ aqueous solution was quickly added to the mixture under vigorous stirring. Stirring continued for another 15 min before the solid product was collected by centrifugation, and vacuum dried at 60 °C overnight.

Material characterization

Field-emission transmission electron microscopy (TEM) and high resolution field emission scanning electron microscopy (FESEM) were performed on a 200 kV JEOL JEM-2010 microscope and a 5 kV JEOL JSM-6700F microscope respectively. XRD patterns were recorded with a Bruker GADDS XRD powder diffractometer using a Cu K_α source (λ = 1.5418 Å) at 40 kV and 30 mA. The Brunauer, Emmett and Teller (BET) surface area and pore size were measured by using a NOVA 4200e Surface Area and Pore Size Analyzer. X-ray photoelectron spectroscopy (XPS) was carried out on a Kratos Axis Ultra DLD spectrometer. All binding energies were referenced to carbon C 1s emission at 284.5 eV.

Open Access Article. Published on 29 June 2015. Downloaded on 12/4/2025 5:40:46 PM.
This article is licensed under a Creative Commons Attribution-NonCommercial 3.0 Unported Licence.

Electrochemical measurements

A catalyst ink was prepared by mixing 30 wt% catalyst, 60 wt% KB and 10 wt% PVDF in an appropriate amount of NMP. For the examination of catalyst morphology evolution, the weight ratio of catalyst : KB : PVDF was changed to 8 : 1 : 1. The mixture was stirred for 24 h to form a uniform dispersion. The ink was then evenly spread on a carbon paper (11 mm in diameter and 146 μm thick) for electrochemical measurements (or onto a 11 mm diameter Ni foam for morphology evolution examinations), and then dried in a vacuum for 8 h at 100 °C.

The dried electrode was weighed and transferred to an argon-filled glove-box (M Braun) where the moisture and oxygen contents were below 0.1 ppm each. Type 2032 button cells (MTI) with perforations on one of the covers were used for the assembly of Li–O_2 cells. Each Li–O_2 cell consisted of a catalyst-loaded carbon electrode, a lithium metal pellet anode (19 mm in diameter, ~0.45 mm thick), a Celgard C480 separator (19 mm in diameter), Whatman glass microfiber paper (GF/B, 19 mm in diameter), and a 0.1 M $LiCF_3SO_3$ in a TEGDME electrolyte. A 19 mm diameter nickel foam was used as the cathode current collector. The assembled cells were placed in a custom-made gas bottle and purged with dry O_2 (Soxal, 99.8%, H_2O < 3 ppm) for 15 min. The O_2 pressure inside the bottle was then set at 1 atm and the bottle was sealed.

The Li–O_2 cells were rested at an open circuit (~3.0 V *vs.* Li/Li^+) for 12 h before any measurement. Tests for electrochemical performance were conducted using a Neware CT-3008 battery tester. The cut-off voltages for discharge and charge were set at 2.2 V and 4.4 V respectively to minimize electrolyte decomposition. Cycle stability was tested at 100 mA g^{-1} for a DOD of 1000 mA h g^{-1}.

For the examination of cathode morphology evolution, a typical cell was disassembled to recover the oxygen electrode after testing. The recovered Ni foam electrode was equilibrated in acetonitrile for 2 h to remove the electrolyte. It was then dried in the glove box and examined by FESEM.

All capacities in this report were normalized by the combined weight of the catalyst and KB carbon. All electrode potentials in this study were referenced to Li/Li^+.

Results and discussion

In the preparation of HMCMS by the hard template method, solid silica particles with a mesoporous shell (Fig. S1A†) were first prepared and then coated with polydopamine from the polymerization of dopamine.[27] Mesoporous microspheres with a hollow interior were formed after calcination of the polydopamine-coated silica in Ar followed by HF etching (Fig. 1A–C). The HMCMS fabricated as such were ~380 nm diameter microspheres with a ~270 nm diameter hollow core and a ~55 nm thick mesoporous shell (Fig. 1A, B and 2A, B). There were a few ruptured microspheres (Fig. 2A and B) produced most likely by the collapse of the carbon shell during the removal of the silica core. These ruptured spheres in Fig. 2B were however useful in revealing the hollow interior of the HMCMS. The AuPt NPs deposited on the HMCMS surface were fairly uniform in size, about 5–6 nm in diameter and without any sign of agglomeration (Fig. 1D–F, 2C, D and S1B†). The reference AuPt NPs prepared without the HMCMS had about the same size but were otherwise severely agglomerated in the absence of a support or capping agent (Fig. S2†).

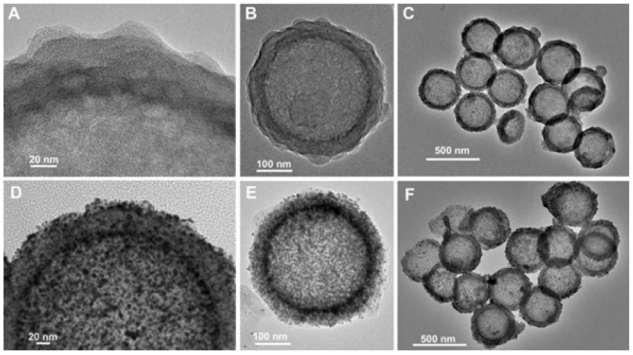

Fig. 1 High resolution TEM images of (A)–(C) HMCMS and (D–F) AuPt/HMCMS composite.

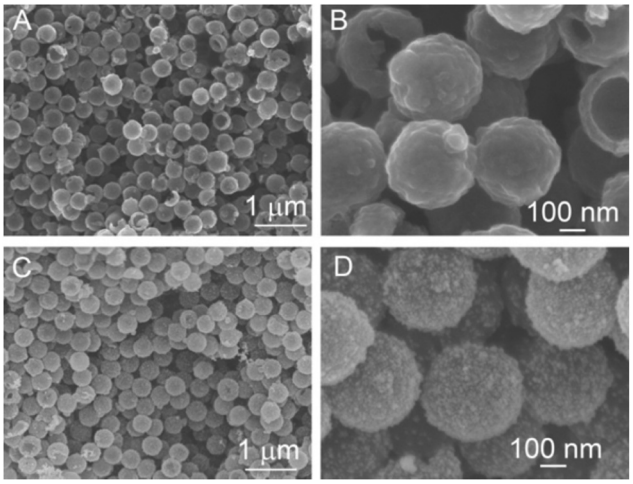

Fig. 2 High resolution SEM images of (A, B) HMCMS and (C, D) AuPt/HMCMS composite.

Nitrogen desorption–adsorption measurements were used to characterize the porosity in HMCMS and the AuPt/HMCMS composite. Typical type IV isotherms were obtained in both cases thereby confirming the presence of mesopores (Fig. S3a and c†). The BET surface areas were 886.1 m^2 g^{-1} (specific pore volume 0.90 cm^3 g^{-1}) for HMCMS and 74.2 m^2 g^{-1} (specific pore volume 0.11 cm^3 g^{-1}) for AuPt/HMCMS. The persistence of a single peak corresponding to a pore diameter of 3.5 nm in the pore size distribution plot (Fig. S3b and d†) suggests that the deposition of AuPt NPs had not significantly affected the mesoporous structure. The decrease in the BET

 This journal is © The Royal Society of Chemistry 2015

Open Access Article. Published on 29 June 2015. Downloaded on 12/4/2025 5:40:46 PM.
This article is licensed under a Creative Commons Attribution-NonCommercial 3.0 Unported Licence.

surface area was caused mostly by an increase in weight from the inclusion of AuPt NPs in the composite, although some of the mesopores in the HMCMS shell could also have been blocked by the AuPt NPs.

The % of AuPt NPs by weight in the composite was estimated by EDX analysis (Fig. S4†). The C, N, Au and Pt contents in the composite determined as such were 33.3 wt%, 2.5 wt%, 32.7 wt% and 31.5 wt% respectively, from which the loading of AuPt NPs in the composite was calculated as ~64 wt%. The atomic ratio of Au to Pt was ~1 : 1.

XRD also confirmed the formation of a 1 : 1 AuPt alloy. Other than a broad diffraction feature in the AuPt/HMCMS composite at about $2\theta = 30°$ attributable to the HMCMS, the other XRD peaks of AuPt NPs and AuPt/HMCMS were largely similar and in agreement with those of the FCC-structured 1 : 1 AuPt alloy (JCPDF card 01-074-5396, $Au_{0.5}Pt_{0.5}$) (Fig. S5†).[28]

High resolution XPS was then used to analyze the surface composition and electron interactions in HMCMS, AuPt NPs and the AuPt/HMCMS composite (Fig. S6†). The two peaks with binding energies of 83.40 eV and 87.05 eV from AuPt/HMCMS could easily be assigned to Au $4f_{7/2}$ and Au $4f_{5/2}$ respectively. The peak locations indicate a negative shift of ~0.3 V from the unsupported AuPt NPs (Fig. S6a†). Likewise the Pt $4f_{7/2}$ and Pt $4f_{5/2}$ peaks of AuPt/HMCMS also shifted negatively by ~0.3 V (Fig. S6b†). These negative shifts may be used to suggest the presence of the metal–support interaction between the HMCMS support and AuPt NPs. The C 1s peaks of AuPt/HMCMS and HMCMS could be deconvoluted into four component peaks at 284.5 eV, 285.5 eV, 286.5 eV and 288.3 eV, attributable to graphitic carbon (C–C π*), C–N, C–OH and C=O species respectively. The presence of nitrogen doping of carbon is suggested by the identification of C–N species, and the C–OH and C=O remnants of polydopamine.[29] The N 1s spectrum also verifies the presence of N in the composite and HMCMS (Fig. S6d†): there are two conspicuous N peaks for HMCMS: pyrrolic N (–N–H) at 399.8 eV and iminic N (=N–)[30,31] at 397.3 eV which clearly originated from polydopamine. The extent of nitrogen doping as estimated from the XPS spectra was 4.2 wt%. The signal-to-noise ratios of the N 1s spectra were quite low, making it difficult to measure the peak shifts between HMCMS and AuPt/HMCMS. However, judging from the shifts of the Au 4f and Pt 4f peaks, there was probably some electron migration from the N sites to the AuPt sites in AuPt/HMCMS. Similar shifts have also been reported for other N-doped composite materials (*e.g.* $MnCo_2O_4$–graphene).[30]

The effectiveness of the catalysts for LOB reactions was evaluated in full LOB test cells using a relatively stable electrolyte (1 M $LiCF_3SO_3$ in TEGDME) to minimize electrolyte decomposition.[32] At a current density of 100 mA g^{-1}, the cell with the AuPt/HMCMS cathode delivered the highest specific capacity and the smallest charge–discharge voltage gap (Fig. 3A). The specific discharge capacity of 6028 mA h g^{-1} was 168% of the capacity of the AuPt NP-only cell (3590 mA h g^{-1}) and 244% of the HMCMS-only cell (2467 mA h g^{-1}). At a capacity of

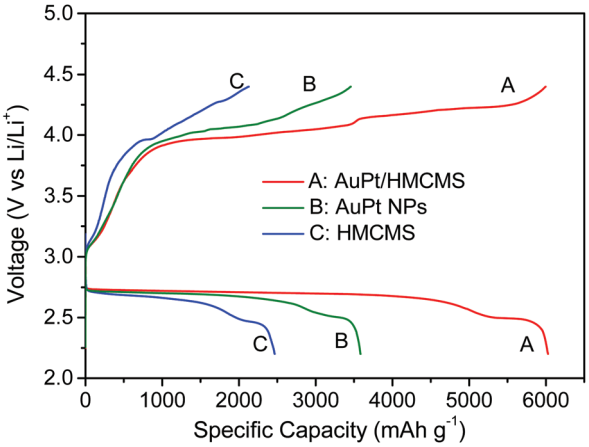

Fig. 3 First cycle discharge–charge curves of full cells with AuPt/HMCMS, AuPt NPs and HMCMS cathode catalysts at 100 mA g^{-1}.

2000 mA h g^{-1}, the voltage gap was 1.28 V for the AuPt/HMCMS cell, 1.41 V for the AuPt NP cell and 1.88 V for the HMCMS cell (Fig. 3). A significant increase in specific capacity and a decrease in the discharge/charge voltage gap therefore suggest the synergy of functions when AuPt and HMCMS were combined to form a composite catalyst. The "storage capacity" for Li_2O_2 of a catalyst is determined by the activity, surface area, pore structure and the free volume of the catalyst.[33] Clearly the deposition of the catalytically more active AuPt NPs in HMCMS had elevated the ORR and OER properties of HMCMS. This merely confirms that AuPt NPs are better electrocatalysts for ORR and OER (higher ORR voltage plateaus and lower OER voltage plateaus). The metal–support interaction which resulted in a net migration of electrons from the support to the metal could also be a factor; although we could not quantify its impact on the kinetics of oxygen electrocatalysis at this point in time. XPS analysis of all electrodes after the first discharge process confirmed that the discharge product was Li_2O_2 (Fig. S7†).[34,35]

The rate performance of LOBs with the AuPt/HMCMS catalyst was evaluated at three current densities (Fig. 4). The discharge capacities at the current densities of 100, 200 and 500 mA g^{-1} were 6028, 5712 and 4619 mA h g^{-1} respectively. There was only a 5% capacity decrease when the current density was doubled from 100 to 200 mA g^{-1}. The capacity decrease for a quintupling of the current density (from 100 to 500 mA g^{-1}) was expectedly higher, at ~23%. These capacity losses were much smaller than catalysts without the dual-pore structure. For example, the capacity of a CNT–RuO_2 core–shell catalyst electrode decreased by 10% when the current density was doubled from 100 to 200 mA g^{-1}, and the decrease was 30% when the current density was quintupled to 500 mA g^{-1}.[24] In another example, Co_3O_4 NPs supported on carbon spheres showed a 50% drop in specific capacity when the current density was doubled from 100 to 200 mA g^{-1}. The capacity decrease escalated to 70% when the current density was increased further to 400 mA g^{-1}.[36]

Open Access Article. Published on 29 June 2015. Downloaded on 12/4/2025 5:40:46 PM.
This article is licensed under a Creative Commons Attribution-NonCommercial 3.0 Unported Licence.

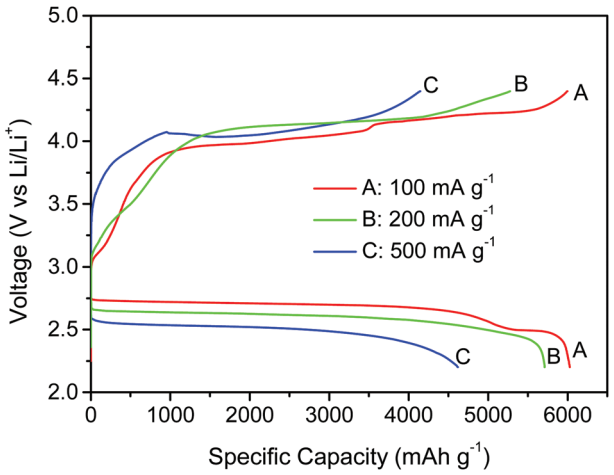

Fig. 4 First cycle discharge–charge curves of full cells with the AuPt/HMCMS cathode catalyst measured at different current densities in the 2.2 V–4.4 V voltage window.

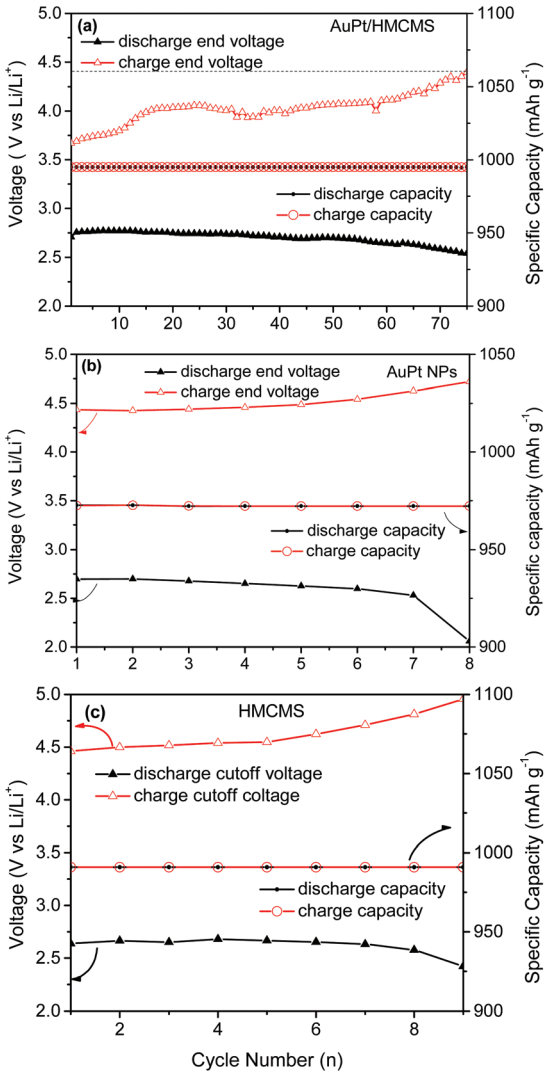

Fig. 5 Cyclability at 100 mA g^{-1} for a DOD of 1000 mA h g^{-1}. (a) AuPt/HMCMS composite; (b) AuPt NPs and (c) HMCMS.

The discharge/charge voltage gaps at 100, 200 and 500 mA g^{-1} were 1.27 V, 1.48 V and 1.53 V respectively. It is worth mentioning that an increase in the voltage gap was caused mainly by the ORR overpotential, which decreased the discharge voltage from 2.71 V at 100 mA g^{-1}, to 2.63 V at 200 mA g^{-1} and 2.52 V at 500 mA g^{-1}, possibly due to the limitations of transport or activation processes at a high current density. On the other hand, the OER overpotential was almost the same and varied relatively insignificantly with the current density. Since the OER process is less affected by the diffusion of reactive species, the measurements there can be used to more accurately reflect the intrinsic activity of the catalyst. Indeed an increase in OER overpotential with current density changes is small compared with other catalysts[24] *e.g.* the increase in OER polarization for a CNT–RuO_2 core–shell catalyst was 150 mV when the current density was increased from 100 to 200 mA g^{-1}, and was 250 mV when the increase was from 200 to 500 mA g^{-1}.[24]

The specific capacity and rate performance of the AuPt/HMCMS cathode were also considerably better than the similarly sized AuPt NPs (~6.8 nm, supported on Vulcan XC 72 carbon black) reported by Yang and coworkers.[22] In that work, the discharge/charge capacities at 60 mA g^{-1} were 840/700 mA h g^{-1} (based on the combined weight of carbon black and AuPt NPs), and reduced to ~700/400 mA h g^{-1} at 150 mA g^{-1}. The voltage gap was 1.5 V at 150 mA g^{-1}.[22] The higher specific capacity and greater rate performance of the AuPt/HMCMS cathode here could be attributed to the combination of a large surface area for catalysis, more facile charge and mass transfer of the HMCMS support, a large volume for Li_2O_2 storage, and the high OER and ORR catalytic activities of the AuPt NPs.

Cell cyclability was tested by discharging and charging a cell repeatedly at 100 mA g^{-1} to a depth of 1000 mA h g^{-1}. Fig. 5 is a plot of discharge and charge cutoff voltages *versus* cycle number. The AuPt/HMCMS cell could be cycled for 75 times before the charge cutoff voltage of 4.4 V was breached. Cells with AuPt NPs and HMCMS catalysts fared much worse, sustaining only 8 cycles before either the discharge cutoff voltage or the charge cut off voltage was exceeded. The cycling performance measurements clearly identified the AuPt/HMCMS composite as the most capable (among the three catalysts) for bifunctional oxygen electrocatalysis in the LOB test environment.

The morphology of the AuPt/HMCMS catalyst in different states of discharge and charge was then examined. For this series of measurements the cell was discharged or charged to a preset cell voltage (2.0 V, 4.0 V, 4.2 V and 4.4 V). The cell was then disassembled to retrieve the cathode for FESEM examination. Discharge to 2.2 V was found to cover the AuPt/HMCMS surface with a film-like discharge product (Fig. 6A). The AuPt NPs were completely hidden from view but there was no sign of the toroid-shaped Li_2O_2 particles reported in some litera-

 This journal is © The Royal Society of Chemistry 2015

Open Access Article. Published on 29 June 2015. Downloaded on 12/4/2025 5:40:46 PM.
This article is licensed under a Creative Commons Attribution-NonCommercial 3.0 Unported Licence.

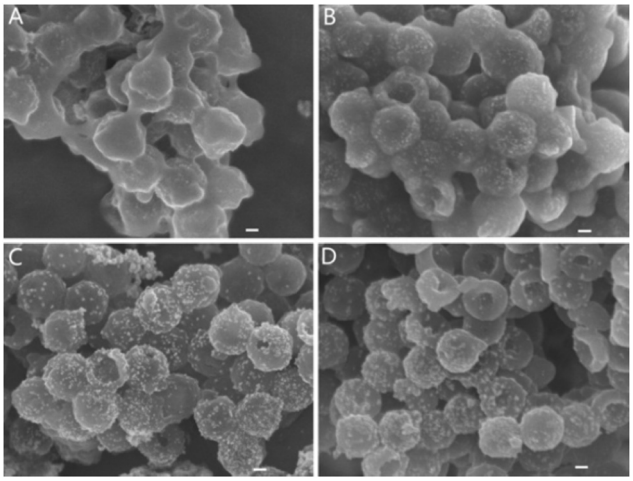

Fig. 6 High resolution SEM images of the electrode with the AuPt/HMCMS catalyst at different cutoff voltages during discharge and charge at 100 mA g^{-1}. (A) 2.2 V, (B) 4.0 V, (C) 4.2 V and (D) 4.4 V. Scale bar is 100 nm.

ture.[6,37] The Li_2O_2 layer was significantly thinner after charging to 4.0 V and many of the AuPt NPs on the HMCMS surface reappeared. These are indications of the partial decomposition of Li_2O_2 (Fig. 6B). At 4.2 V, the morphology of the original composite catalyst was nearly fully restored. The morphology at 4.4 V was almost identical to that at 4.2 V, confirming that the decomposition of the Li_2O_2 was almost complete at 4.2 V. By measuring the size difference between the spheroids at 2.2 V and 4.4 V, the thickness of the Li_2O_2 layer was estimated to be about 20–25 nm.

It is interesting to compare the morphology evolution of the AuPt/HMCMS catalyst with that of HMCMS which engendered the dual-pore structure. A film-like Li_2O_2 deposit was again formed at 2.2 V (Fig. 7A). The Li_2O_2 film was also thinned upon charging but the decomposition of the Li_2O_2 layer did not appear to be as facile and as extensive as the AuPt/HMCMS catalyst. Hence the Li_2O_2 film was still thick at 4.2 V and was not even completely removed at 4.4 V.

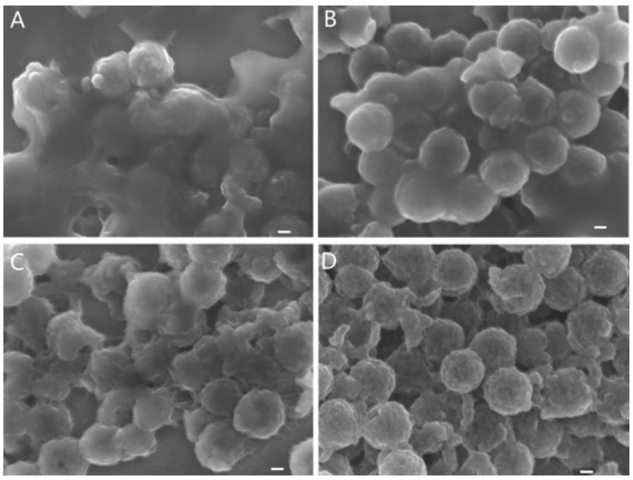

Fig. 7 High resolution SEM images of the electrode with the HMCMS catalyst at different cutoff voltages during discharge–charge at 100 mA g^{-1}. (A) 2.2 V, (B) 4.0 V, (C) 4.2 V and (D) 4.4 V. Scale bar is 100 nm.

The morphology examination of the catalysts indicated that the HMCMS architecture had exerted a strong influence on the discharge product morphology – instead of toroidal Li_2O_2 which usually indicates a lack of affinity between the deposit and the substrate, Li_2O_2 was formed as a uniform thin film enveloping the HMCMS surface. The shape-conforming thin film maximized the contact with the underlying conductive (carbon) surface, thereby improving the charge transfer between Li_2O_2 and carbon in the discharge reaction. Li_2O_2 decomposition was made more facile especially in the presence of catalytically more active components such as AuPt NPs. The reason for the formation of the film-like Li_2O_2 layer is not known although it is tempting to associate it with nitrogen doping and the dual pore architecture of the HMCMS. The *in situ* N-doping of HMCMS through the polydopamine route allowed nitrogen atoms to be uniformly dispersed in the carbon skeleton. The presence of nitrogen atoms in carbon not only improved the substrate conductivity, but also rendered the carbon more catalytically active for ORR.[33] A more uniform distribution of catalytically active sites could stimulate conformal deposition resulting in a film-like deposit on the HMCMS surface. Furthermore, the unimpeded transport of Li^+, electrons and oxygen through the mesopores of the HMCMS shell also assisted in the deposition of Li_2O_2 as a uniform film. The AuPt NPs in the composite contributed more significantly to OER and hence solid Li_2O_2 could be decomposed at lower voltages on the composite catalyst than on the pristine HMCMS catalyst.

Conclusions

Encouraging results were obtained by using mesoporous nitrogen-doped carbon microspheres with a hollow interior as the conducting catalyst support for 1 : 1 AuPt NPs in nonaqueous LOBs. Relative to pristine HMCMS and unsupported AuPt NPs, charge and discharge overpotentials were lower, and specific capacity, rate performance and cycle life were higher for LOBs with the AuPt/HMCMS composite catalyst. Discharge and charge specific capacities as high as 6028 and 6000 mA h g^{-1} were possible at a current density of 100 mA g^{-1}, where the discharge–charge voltage gap was only 1.27 V. A cell with the composite catalyst could be cycled 75 times at a DOD of 1000 mA h g^{-1} without the charge cut-off voltage exceeding 4.4 V. The discharge capacity decreased only by 5% when the current density was doubled, and by 23% when the current density was quintupled. The good electrochemical performance of the AuPt/HMCMS catalyst correlates well with the dual-pore (mesopore/macropore) structure of the HMCMS and the good ORR/OER catalytic activities of AuPt NPs. Nitrogen doping of the mesoporous carbon spheres increased the conductivity of the carbon support, while the dual pore architecture supported a

Open Access Article. Published on 29 June 2015. Downloaded on 12/4/2025 5:40:46 PM.
This article is licensed under a Creative Commons Attribution-NonCommercial 3.0 Unported Licence.

more facile transport of Li^+ and the electrolyte, and oxygen diffusion. The Li_2O_2 formed on the AuPt/HMCMS surface was film-like and as such was easier to decompose during recharge. These measurements indicate that HMCMS is a good catalyst support to use for increasing the catalyst effectiveness for LOB applications.

Acknowledgements

This research was financially supported by the research grant (R-265-000-436-305) of Advanced Energy Storage Programme from the SERC, Singapore. M. H. Lu acknowledges the National University of Singapore for her research scholarship.

References

1 K. M. Abraham, *J. Electrochem. Soc.*, 1996, **143**, 1.
2 Y.-C. Lu, B. M. Gallant, D. G. Kwabi, J. R. Harding, R. R. Mitchell, M. S. Whittingham and S.-H. Yang, *Energy Environ. Sci.*, 2013, **6**, 750.
3 J.-S. Lee, S. T. Kim, R. Cao, N.-S. Choi, M. Liu, K. T. Lee and J. Cho, *Adv. Energy Mater.*, 2011, **1**, 34.
4 X.-h. Yang, P. He and Y.-y. Xia, *Electrochem. Commun.*, 2009, **11**, 1127.
5 J.-B. Park, J. Lee, C. S. Yoon and Y.-K. Sun, *ACS Appl. Mater. Interfaces*, 2013, **5**, 13426.
6 Z.-L. Wang, D. Xu, J.-J. Xu, L.-L. Zhang and X.-B. Zhang, *Adv. Funct. Mater.*, 2012, **22**, 3699.
7 Z. Guo, D. Zhou, X. Dong, Z. Qiu, Y. Wang and Y. Yao, *Adv. Mater.*, 2013, **25**, 5668.
8 X. Lin, L. Zhou, T. Huang and A. Yu, *J. Mater. Chem. A*, 2013, **1**, 1239.
9 S. Liu, Z. Wang, C. Yu, Z. Zhao, X. Fan, Z. Ling and J. Qiu, *J. Mater. Chem. A*, 2013, **1**, 12033.
10 J. Xiao, D. Mei, X. Li, W. Xu, D. Wang, G. L. Graff, W. D. Bennett, Z. Nie, L. V. Saraf, I. A. Aksay, J. Liu and J.-G. Zhang, *Nano Lett.*, 2011, **11**, 5071.
11 B. Sun, X. Huang, S. Chen, P. Munroe and G. Wang, *Nano Lett.*, 2014, **14**, 3145.
12 H. Nie, H. Zhang, Y. Zhang, T. Liu, J. Li and Q. Lai, *Nanoscale*, 2013, **5**, 8484.
13 R. Mi, H. Liu, H. Wang, K.-W. Wong, J. Mei, Y. Chen, W.-M. Lau and H. Yan, *Carbon*, 2014, **67**, 744.
14 Y. Li, J. Wang, X. Li, J. Liu, D. Geng, J. Yang, R. Li and X. Sun, *Electrochem. Commun.*, 2011, **13**, 668.
15 K. N. Wood, R. O'Hayre and S. Pylypenko, *Energy Environ. Sci.*, 2014, **7**, 1212.
16 Y. Li, J. Wang, X. Li, J. Liu, D. Geng, J. Yang, R. Li and X. Sun, *Electrochem. Commun.*, 2011, **13**, 668.
17 D. Zhu, L. Zhang, M. Song, X. Wang and Y. Chen, *Chem. Commun.*, 2013, **49**, 9573.
18 Y. Shen, D. Sun, L. Yu, W. Zhang, Y. Shang, H. Tang, J. Wu, A. Cao and Y. Huang, *Carbon*, 2013, **62**, 288.
19 H. Liu and Y. Xing, *Electrochem. Commun.*, 2011, **13**, 646.
20 B. Sun, P. Munroe and G. Wang, *Sci. Rep.*, 2013, **3**, 2247.
21 H.-G. Jung, Y. S. Jeong, J.-B. Park, Y.-K. Sun, B. Scrosati and Y. J. Lee, *ACS Nano*, 2013, **7**, 3532.
22 Y.-C. Lu, Z. Xu, H. A. Gasteiger, S. Chen, K. Hamad-Schifferli and S.-H. Yang, *J. Am. Chem. Soc.*, 2010, **132**, 12170.
23 D. Su, H.-S. Kim, W.-S. Kim and G. Wang, *J. Power Sources*, 2013, **244**, 488.
24 Z. Jian, P. Liu, F. Li, P. He, X. Guo, M. Chen and H. Zhou, *Angew. Chem., Int. Ed.*, 2014, **53**, 442.
25 E. Yilmaz, C. Yogi, K. Yamanaka, T. Ohta and H. R. Byon, *Nano Lett.*, 2013, **13**, 4679.
26 J. Sun, J. Zhang, M. Zhang, M. Antonietti, X. Fu and X. Wang, *Nat. Commun.*, 2012, 1139.
27 C. Xiao, X. Chu, Y. Yang, X. Li, X. Zhang and J. Chen, *Biosens. Bioelectron.*, 2011, **26**, 2934.
28 A. S. Darling, R. A. Mintern and J. C. Chaston, *J. Inst. Met.*, 1953, **18**, 125.
29 B. J. Schultz, R. V. Dennis, J. P. Aldinger, C. Jaye, X. Wang, D. A. Fischer, A. N. Cartwright and S. Banerjee, *RSC Adv.*, 2014, **4**, 634.
30 Y. Liang, H. Wang, J. Zhou, Y. Li, J. Wang, T. Regier and H. Dai, *J. Am. Chem. Soc.*, 2012, **134**, 3517.
31 C. Xu, M. Tian, L. Liu, H. Zou, L. Zhang and W. Wang, *J. Electrochem. Soc.*, 2012, **159**, D217.
32 H.-G. Jung, J. Hassoun, J.-B. Park, Y.-K. Sun and B. Scrosati, *Nat. Chem.*, 2012, **4**, 579.
33 S. H. Oh, R. Black, E. Pomerantseva, J.-H. Lee and L. F. Nazar, *Nat. Chem.*, 2012, **4**, 1004.
34 P. Du, J. Lu, K. C. Lau, X. Luo, J. Bareno, X. Zhang, Y. Ren, Z. Zhang, L. A. Curtiss, Y.-K. Sun and K. Amine, *Phys. Chem. Chem. Phys.*, 2013, **15**, 5572.
35 Y. Qin, J. Lu, P. Du, Z. Chen, Y. Ren, T. Wu, J. T. Miller, J. Wen, D. J. Miller, Z. Zhang and K. Amine, *Energy Environ. Sci.*, 2013, **6**, 519.
36 C. S. Park, K. S. Kim and Y. J. Park, *J. Power Sources*, 2013, **244**, 72.
37 D. Zhai, H. H. Wang, J. Yang, K. C. Lau, K. Li, K. Amine and L. A. Curtiss, *J. Am. Chem. Soc.*, 2013, **135**, 15364.

 This journal is © The Royal Society of Chemistry 2015